Key Points:
- Shelf current in the northern South China Sea shows extensive interannual variability
- Terrestrial forcings determines interannual variability of hydrographic properties of coastal oceans to the west of Pearl River Estuary
- The shelf current shows notable asymmetric responses to interannual changes of winds over the shelf

Correspondence to:
Z. Liu and Z. Cai,
liuzq@sustech.edu.cn;
zycai@um.edu.mo

Author Contributions:
Conceptualization: Zhiqiang Liu, Zhongya Cai
Data curation: Yongfei Deng, Qi Quan
Formal analysis: Yongfei Deng, Yuxin Lin
Funding acquisition: Zhiqiang Liu, Tingting Zu, Jianyu Hu, Jianping Gan, Zhongya Cai
Investigation: Yongfei Deng, Zhiqiang Liu
Methodology: Yongfei Deng, Zhiqiang Liu, Zhongya Cai
Project Administration: Zhiqiang Liu
Resources: Zhiqiang Liu, Jianping Gan
Software: Zhiqiang Liu, Zhongya Cai
Supervision: Zhiqiang Liu, Zhongya Cai
Validation: Yongfei Deng, Zhibing Li
Visualization: Yongfei Deng, Zhiqiang Liu, Yuxin Lin
Writing – original draft: Yongfei Deng
Writing – review & editing: Zhiqiang Liu, Tingting Zu, Jianyu Hu, Jianping Gan, Zhibing Li, Qi Quan, Zhongya Cai

Climatic Controls on the Interannual Variability of Shelf Circulation in the Northern South China Sea

Yongfei Deng[1] , Zhiqiang Liu[1,2] , Tingting Zu[2,3], Jianyu Hu[4] , Jianping Gan[5] , Yuxin Lin[1], Zhibing Li[1], Qi Quan[1,6] , and Zhongya Cai[7]

[1]Department of Ocean Science and Engineering, Southern University of Science and Technology, Shenzhen, China, [2]Southern Marine Science and Engineering Guangdong Laboratory (Guangzhou), Guangzhou, China, [3]State Key Laboratory of Tropical Oceanography, South China Sea Institute of Oceanology, Chinese Academy of Sciences, Guangzhou, China, [4]State Key Laboratory of Marine Environmental Science, College of Ocean and Earth Sciences, Xiamen University, Xiamen, China, [5]Department of Ocean Science and Mathematics, Center for Ocean Research in Hong Kong and Macau, Hong Kong University of Science and Technology, Hong Kong, China, [6]State Key Laboratory of Estuarine and Coastal Research, East China Normal University, Shanghai, China, [7]State Key Laboratory of Internet of Things for Smart City, Department of Civil and Environmental Engineering, University of Macau, Macau, China

Abstract We comprehensively investigate the interannual variability of multi-scale motions in the northern South China Sea (NSCS) and associated influences from the terrestrial, atmospheric, and oceanic processes over the period 1994–2018 based on observations and a numerical simulation. We find that the interannual variabilities of the NSCS circulation and hydrographic properties, in the form of a cross-scale interactive dynamic system, are sensitive to the tropical climate variability represented by the El Niño–Southern Oscillation (ENSO). In coastal areas with less than 30 m depth, the anomalous warm (cold) and less (more) saline waters are regulated by the rate of Pearl River discharge due to the predominant precipitation (evaporation) and positive (negative) heat-flux anomaly in the Pearl River catchment in El Niño (La Niña) years. Controlled by the interannual variabilities of slope current and atmospheric forcings, the shelf current at 30–200 m depth responds asymmetrically to the ENSO, which establishes a stronger northeastward flow anomaly in El Niño years than the southwestward flow anomaly in La Niña years. We further show that the interannual variability of the slope current is jointly governed by the atmospheric and oceanic processes that tend to offset each other in interannual timescales. In particular, the weakened (strengthened) cyclonic wind stress curl over the ocean basin tends to moderate (intensify) the slope current in the NSCS, while this process is mitigated by the stronger (weaker) Kuroshio intrusion in El Niño (La Niña) years.

Plain Language Summary The oceanic circulations and biogeochemical processes of shelf seas of the world's oceans have long been recognized to be concurrently impacted by the terrestrial, oceanic, and atmospheric forcings. However, the climatic controls and respective function of those forcings in regulating the interannual variability of shelf circulations in the northern South China Sea (NSCS) have not been thoroughly investigated. This research comprehensively studies the interannual variabilities and joint functions of those forcings in the NSCS. This research relies on valuable long-term observations and well-validated numerical simulation, and demonstrates that hydrographic properties in the coastal seas to the west of the Pearl River Estuary (PRE) are sensitive to the interannual variability of terrestrial forcings sourced from the Pearl River catchment. A large volume of warm and fresh waters is established when the extensive air-sea-land interactions in and around the southern China notably elevate the riverine discharges in El Niño years. Shelf circulations are mainly influenced by interannual changes of the prevailing winds, which drive northeastward shelf current anomalies in El Niño years. The slope current illustrates a southwestward anomaly, elevates the shoreward cross-shelf pressure gradient force and strengthens the northeastward anomaly of shelf current in El Niño years.

1. Introduction

Circulation in the northern South China Sea (NSCS) is composed by cross-scale interactive estuary–shelf–slope currents (Figure 1), and has long been found to significantly vary on interannual timescales associated with the tropical climate variability represented by the El Niño–Southern Oscillation (ENSO) (Lui et al., 2020; Qian et al., 2018), whose impact is conveyed into the South China Sea (SCS) through both atmospheric (e.g., B. Wang et al., 2000) and oceanic pathways (Qu et al., 2004; C. Z. Wang et al., 2006; Y. G. Wang et al., 2006). It has long
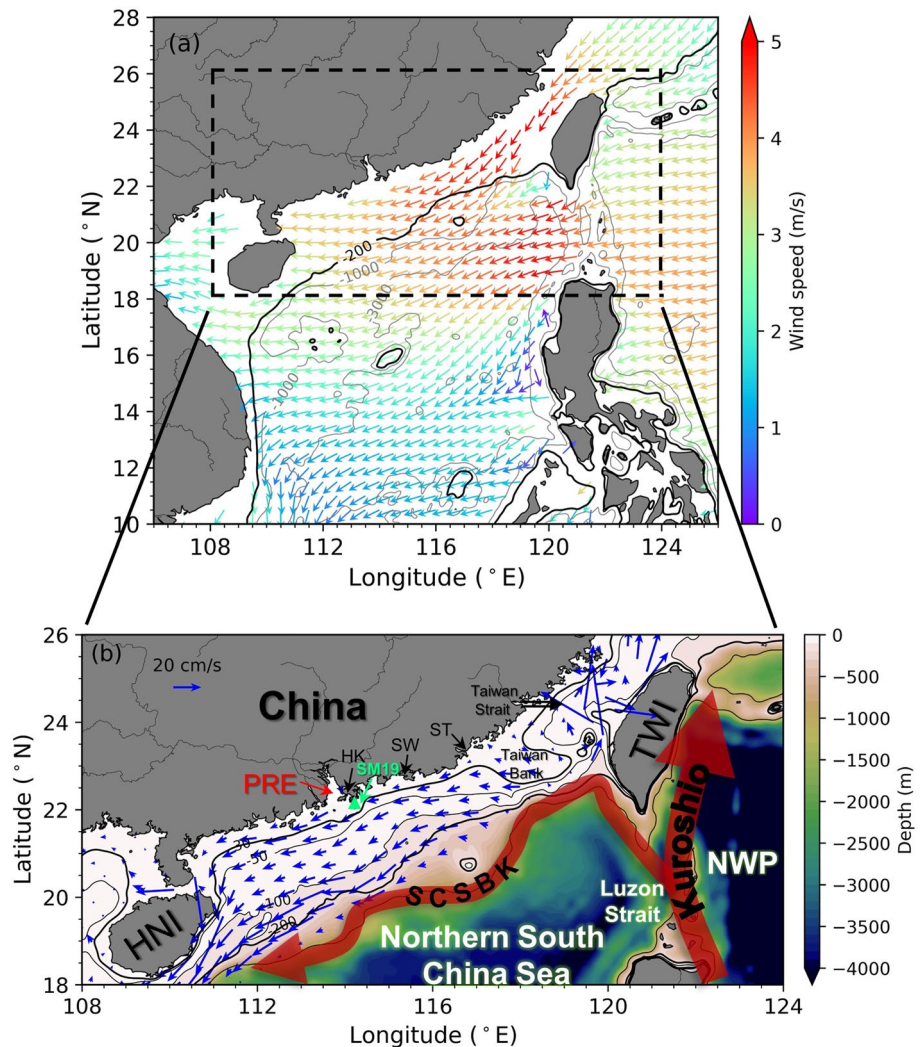
Figure 1. (a) Climatological wind-velocity vectors from ERA5 at 10 m over the South China Sea (SCS) surface during the period 1994–2018. Black and gray contours indicate the 200, 1,000, and 3,000 m isobaths. (b) Bathymetry and climatological circulation in the northern SCS shelf and slope. The shelf current shown in blue arrows is extracted from the numerical simulation and averaged over the 25-year period (1994–2018). Black contours indicate the 30, 50, 100, 200, and 1,000 m isobaths. NWP: northwestern Pacific Ocean; PRE: Pearl River Estuary; HK: Hong Kong; SW: Shanwei; ST: Shantou; TWI: Taiwan Island; HNI: Hainan Island; SCSBK: SCS branch of Kuroshio. The green triangle indicates the hydrographic measurement site SM19. The bathymetry data are from ETOPO-1 (Amante & Eakins, 2009).

been recognized that the responses of shelf circulation to the ENSO greatly affect the regional biogeochemical processes, for example, the long-term field observations in Qian et al. (2018) clearly show extensive interannual variabilities of dissolved inorganic nitrogen (DIN) and dissolved oxygen (DO) in the coastal seas neighboring the Pearl River Estuary (PRE). Lui et al. (2020) further rationalized that these variabilities are critically determined by the remote impact from the ENSO by showing that anoxic condition is prone to be established in La Niña years. This later research, by contrasting the interannual variabilities of hydrographic properties, nutrients and DO observations in the coastal seas and the central basin of the NSCS, further indicates that ENSO could impact the interannual variabilities of shelf waters through the oceanic pathway established by Kuroshio intrusion from the Luzon Strait. However, the responses of shelf current to ENSO through the atmospheric and oceanic pathways have yet been comprehensively investigated.

The ENSO establishes an anomalous anti-cyclonic (cyclonic) wind anomaly in the lower troposphere over the northwestern Pacific Ocean through westward propagating atmospheric Rossby waves from the tropical central Pacific Ocean (B. Wang et al., 2000). The weakened northeasterly winds due to the anti-cyclonic anomalies in

El Niño years reduce the cold air and water advection from higher latitudes, thereby increasing the sea-surface temperature (SST) in the SCS (e.g., G. H. Fang et al., 2006; W. D. Fang et al., 2006). In the oceanic pathway, the Luzon Strait is the major entrance of Kuroshio water intrusions into the SCS (Figure 1b). These water intrusions convey the ENSO signal into the SCS through heat advection, especially in winter (Qu et al., 2004). With the aids of these atmospheric and oceanic forcings, SST (C. L. Liu et al., 2020; N. Liu et al., 2020; Z. Q. Liu et al., 2020) and the upper ocean heat content increase (decrease) (Q. Liu et al., 2011; Yan et al., 2010) during El Niño (La Niña) years, while surface water converges (diverges) and sea level increases (decreases) in the central basin of the SCS (W. D. Fang et al., 2014; Rong et al., 2007). The basin-scale SCS circulation varies with the sea-level changes and favors anomalous anticyclonic (AAC) (cyclonic) currents in El Niño (La Niña) years (G. H. Fang et al., 2006; W. D. Fang et al., 2006; C. Z. Wang et al., 2006; Y. G. Wang et al., 2006). Anticyclonic circulation anomaly accompanied with weakened cyclonically circulating SCS western boundary current (i.e., SCSWBC) is evident in the southern SCS in El Niño years (Quan et al., 2016; Q. Wang et al., 2020; T. Zu et al., 2018), while a concurrent cyclonic circulation anomaly is evident in the NSCS and an eastward cross-basin current is formed in the middle of the basin (Sun & Lan, 2021; Q. Wang et al., 2020).

The majority of these earlier studies focused on the basin-scale circulation, while the interannual variability of the NSCS shelf circulation and its associated mechanisms received less attention. Long-term estimations of the along- and cross-shelf volume transports using satellite-altimetry data reveal significant interannual variabilities and the influence of ENSO (J. Liu et al., 2018; Zhu et al., 2015). The notable interannual variability of the shelf circulation is also indicated by the summer coastal upwelling. For example, Jing et al. (2011) suggested that the anomalous strengthened coastal upwelling east of the PRE in the summer of 1998 was highly related with the 1997/1998 El Niño event, while C. L. Liu et al. (2020), N. Liu et al. (2020), and Z. Q. Liu et al. (2020) revealed a stronger northeastward shelf-current anomaly in El Niño years. However, the atmospheric forcing variabilities, greatly influencing the expansion of the buoyant plume from the PRE (Ou et al., 2009) and the slope current connecting with the Kuroshio intrusion in the Luzon Strait (Hong & Wang, 2008; Xue et al., 2004; Yuan et al., 2007, 2009), are yet to be comprehensively investigated. The dynamical response of the NSCS circulation to the climate variability represented by ENSO remains largely unclear due to the joint controls of the buoyancy plume, regional atmospheric fluxes, and remote Kuroshio intrusion (Shu et al., 2018), yet, the function mechanisms of those jointly imposed forcings, which are focus of this current research, are not thoroughly investigated.

In this study, we investigate the interannual variability of the NSCS shelf circulation by combing results from long-term observations and a well-validated high-resolution ocean model. We discuss the interannual variability of the shelf current in response to regional and remote forcings associated with ENSO. The remainder of this paper is organized as follows: Section 2 introduces observational data and the numerical model configuration. Section 3 discusses the observed and simulated characteristics of the NSCS shelf circulation in El Niño and La Niña years. Section 4 presents the analysis of the internal and external forcings that govern the interannual variability of the NSCS shelf circulation. Section 5 concludes this research.

2. Ocean Model and Observations

2.1. Numerical Implementation and Dynamical Configuration

The Regional Ocean Modeling System (Shchepetkin & McWilliams, 2005) was used for conducting the simulation. Similar to J. P. Gan et al. (2015), the model domain covered the NSCS shelf (Figure 1b) with a spatially varying horizontal resolution (∼2.0–3.0 km). We discretized the water column into 30 levels using the terrain-following *s*-coordinate based on the algorithm of Song and Haidvogel (1994). A higher resolution was adopted in the surface and bottom boundary layers to better resolve the critical processes therein, and in the coastal seas to the shoreward of the 30 m isobath, for example, the highest vertical resolution in those two layers is smaller than 0.1 m. The level-2.5 turbulence-closure scheme of Mellor and Yamada (1982) was adopted for solving the turbulent mixing and diffusion in the water column. The horizontal momentum advection was solved by a third-order upstream scheme, and a fourth-order centered scheme was adopted for solving the vertical momentum advection. The recursive multidimensional positive definite advection transport algorithm (Smolarkiewicz, 1984), which includes anti-diffusive velocities for correcting tracer advection, was used for solving the horizontal and vertical transports of temperature and salinity.

Table 1
Detailed Information on the Different SST Data Sets Used for Model Validation

Data set	Spatial resolution	Time resolution	Period[a]	Institution	Type
GHRSST (G1SST)	0.01°	Daily	2011–2016	NASA JPL	Merged
UKMO-OSTIA	0.05°	Daily	2007–2018	UK Met Office	Merged
HadISST	1°	Monthly	1994–2018	Met Office Hadley Centre	Merged
NOAA Global Coral Bleaching Monitoring	5 km	Monthly	1994–2018	NOAA Coral Reef Watch program	Merged
ARMOR3D	0.25°	Monthly	1994–2018	CMEMS	Merged
ERSST v4	2°	Monthly	1994–2018	NOAA	In situ
ERSST v5	2°	Monthly	1994–2018	NOAA	In situ
MODIS	4 km	Monthly	2003–2018	NOAA	Satellite-derived
AMSR-E	0.25°	Daily	2002–2011	NOAA	Satellite-derived
AVHRR v2.1	0.25°	Daily	1994–2018	NOAA NCEI	Satellite-derived
Pathfinder v 5.2	4 km	Monthly	1994–2012	NOAA NCEI	Satellite-derived

[a]The period is the longest time range covering our study, instead of the data available time.

We nested the simulation with the Hybrid Coordinate Ocean Model and the Navy Coupled Ocean Data Assimilation (HYCOM + NCODA) global 1/12° analysis (GLBv0.08; https://www.hycom.org/), with a 3-hourly temporal interval. Tidal forcing was superimposed through the dual-wave permitting open boundary condition of Liu and Gan (2016). This scheme effectively exerts the jointly imposed tidal and sub-tidal forces with consistent schemes for barotropic and baroclinic velocities and hydrographic properties (Liu & Gan, 2020). We used the hourly atmospheric forcing from the fifth-generation atmospheric reanalysis data set (ERA5) maintained and provided by the European Centre for Medium-Range Weather Forecasts (ECMWFs). We imposed nine major constituents of the semidiurnal (i.e., M_2, S_2, K_2, and N_2) and diurnal (i.e., K_1, O_1, P_1, and Q_1) tides, as well as one of the M_4 tide from the nonlinearity of the predominating M_2 constituent over the shelf in the vicinity of the PRE (Mao et al., 2004). These harmonic constants were inverted from remotely sensed long-term sea-level anomaly (SLA) variations using the Oregon Tide Inverse Software (Egbert & Erofeeva, 2002) of T. T. Zu et al. (2008). The intensity of the riverine discharge rate from the Pearl River recorded by the Chinese Ministry of Water Resources was imposed for forcing the simulation at a daily resolution. We performed the simulations to resolve the interannual variability of the shelf circulation in the 25-year 1994–2018 period.

2.2. Observations

To facilitate further analyses, we used observations including multiple-source remotely sensed SST (see Table 1 for detailed information), satellite-altimetry SLA, and the long-term in situ hydrographic sampling of the Environmental Protection Department of the Hong Kong Special Administrative Region. The hydrographic (i.e., temperature and salinity) data used in this research were observed at the SM19 station (22° 9.211′ N, 114° 13.077′ E; Figure 1b), where the water depth is 24 m and a long-term monthly hydrographic measurement was performed by a conductivity–temperature–depth probe and covered the 1994–2018 period. Temperature and salinity were recorded near (i.e., 1 m below) the sea surface and near (i.e., 1 m above) the seabed, respectively. The gridded SLA and corresponding geostrophic velocities (at 0.25° spatial resolution) from the Copernicus Marine Environment Monitoring Service (CMEMS) were used for investigating the slope current in the sea area seaward of the 200-m isobath.

The interannual variabilities of the atmospheric forcings in 1994–2018 were also analyzed based on the monthly mean wind at 10 m above the sea/land surface, net heat flux, 2 m air temperature and evaporation–precipitation (E–P) from the ECMWF ERA5 data set. We categorized the El Niño and La Niña years by using the Oceanic Niño Index (ONI) from the Climate Prediction Center of National Oceanic and Atmospheric Administration (NOAA), that is, the years with annual mean ONI value higher (lower) than 0.4°C (−0.4°C) as El Niño (La Niña) years. The years 1994, 1997, 2002, 2004, and 2015 were thereby defined as El Niño years, while the years 1996, 1999, 2000, 2007, 2008, 2010, and 2011 were defined as La Niña years. We did not consider the ENSO diversity (i.e., central and eastern Pacific El Niño) in this research due to the limited study period.

3. Observed and Simulated Interannual Variability of the NSCS Shelf Circulation

3.1. Model Validation

The simulation captured well the predominant horizontal pattern of the remotely sensed SST (Figures 2a and 2b). The low temperature signal in the coastal region east of the PRE indicates intensified upwelling of deep water from the outer shelf, as presented in our earlier studies (N. Liu et al., 2020; N. Liu et al., 2020; Z. Q. Liu et al., 2020). Temporally, the interannual variability of the simulated SST was also highly consistent with the observations (Figure 2c). The simulated SST lied reasonably within the range of uncertainty of the ensemble data, with 0.93 correlation coefficient (R) and ~0.08°C root-mean-square error (RMSE). The temporal variability of the observed and simulated SSTs also exhibited correlation with that of the ONI ($R = 0.39$; $p = 0.05$), indicating a possible thermal impact on the shelf region due to ENSO. Additionally, the SLA from satellite altimetry and numerical simulation was horizontally averaged across the shelf at depths greater than 200 m (Figure 2d). The high R (i.e., 0.72; $p < 0.001$) and low RMSE (i.e., ~0.01 m) suggested that the simulated interannual SLA fluctuation agrees well with the satellite-altimetry observations.

Given that the shelf circulation in the NSCS is also modulated by the buoyant waters from the PRE, the simulation was further validated by comparison with the annually averaged potential density, computed from long-term continuous in situ observations of temperature and salinity in the water column (Figure 2e) at the SM19 site (Figure 1b). High correlation coefficients with values of 0.82 and 0.60 were found between the simulated and observed potential density anomalies near the surface and seabed, respectively. The surface-water density decreased (i.e., water became warmer and less saline) in El Niño years (e.g., 1994, 2001, 2016), while it increased (i.e., water became colder and more saline) in La Niña years (e.g., 2007, 2010, 2011). Conversely, the seabed-water density exhibited an opposite trend, that is, it increased in El Niño years (e.g., 2002, 2015) and decreased in La Niña years (e.g., 1999).

3.2. NSCS Shelf Circulation in El Niño and La Niña Years

The previous comparisons showed that the simulation resolved well the interannual variation of the NSCS shelf current, not only regarding its barotropic component represented by the SLA variations, but also regarding its baroclinic component related to the spatiotemporal variability of potential density in the coastal areas and SST over the shelf. We further explored the responses of the NSCS shelf circulation to ENSO. Figure 3 shows the horizontal maps of anomalies in temperature, salinity, and flow field in the upper (i.e., 30 m below the sea surface) and lower (i.e., 30 m above the seabed) layers of the NSCS shelf. The anomalies were computed with respect to the 1994–2018 average climatology of the parameters, and these maps were composited for the El Niño and La Niña years, respectively. In the upper layer, an overall warming (cooling) anomaly with less (more) saline waters was evident in El Niño (La Niña) years, particularly across the coastal areas with less than 30 m depth (Figures 3a–3f). The shelf current generally showed a northeastward (southwestward) flow anomaly in El Niño (La Niña) years, and intensities of these anomalies in coastal areas with depth less than 30 m depth are weaker than those to the seaward from the 30–200 m isobath. The above suggests that the buoyant impact on the neighboring PRE possibly overrode the regional atmospheric forcing changes in the coastal areas to the shoreward from the 30 m isobath, where the buoyancy effect of warmer and less saline waters weakened the northeastward flow anomaly in El Niño years (Figure 3c). Conversely, in La Niña years, the southwestward flow anomaly was reduced or even reversed in the coastal areas west of the PRE (Figure 3f), possibly due to the reduced buoyant water discharge. This contrasting distributions of hydrographic properties and shelf current suggest that the buoyant impact from the neighboring PRE should be further explored; thus, we perform in the following.

A notable asymmetrical response of the shelf circulation to ENSO was evident over the shelf and seaward of the 30-m isobath, and the velocity anomaly in El Niño years was higher than that in La Niña years (Figures 3c and 3f). Meanwhile, in El Niño years, the upper layer salinity revealed a significant plume of less saline water off the coast, east of the PRE and southwest of the Taiwan Bank (Figure 3b). The northeastward velocity anomaly in El Niño years (Figure 3c) was consistent with the changes in hydrographic properties. Given that the seasonal climatology of the shelf circulation of the NSCS (not shown) is composed by an extensive northeastward flow and southwestward flow in summer and winter (e.g., Shu et al., 2018), respectively, a northeastward velocity anomaly facilitated an eastward extension of the buoyant plume, as well as the cross-shelf intrusion of more saline waters off the coastline and northeast of Shantou, in summer, and weakened the southwestward transport of
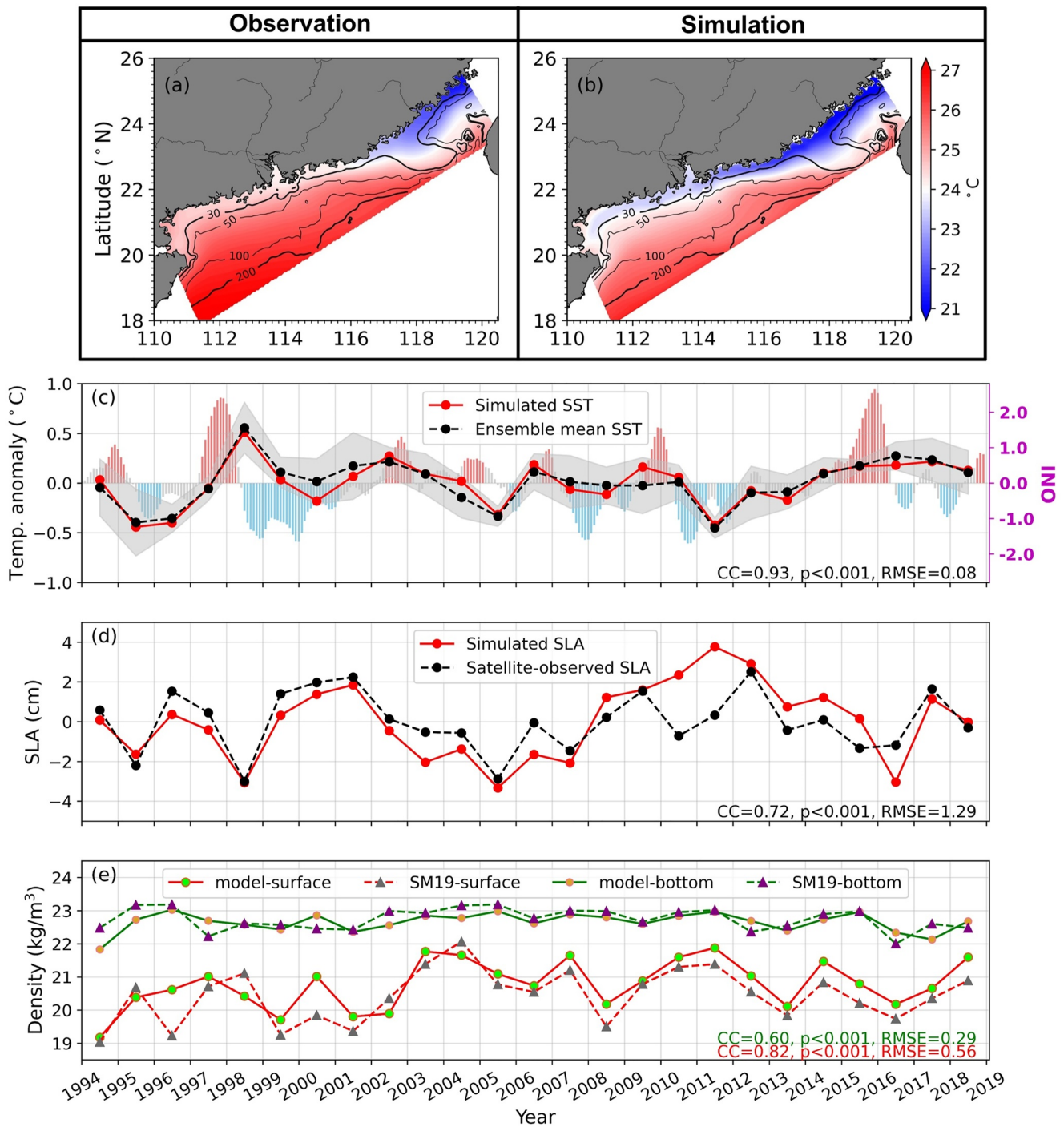
Figure 2. (a and b) 25-year averaged remotely sensed and simulated sea-surface temperatures (SSTs). Black contours indicate the 30, 50, 100, and 200 m isobaths. The remotely sensed SST data are from the National Oceanic and Atmospheric Administration coral reef watch program (see Table 1). (c) Time series of the annually averaged simulated and observed SST anomalies, averaged over the domain shown in (a and b). The black line is the ensemble of the multi-source SST data sets (see Table 1). The gray area indicates two standard deviations of the observed SST. The bars (red: El Niño events; blue: La Niña events) indicate the monthly averaged Oceanic Niño Index (ONI). (d) Time series of the simulated sea-level anomaly (SLA) and observed SLA over the domain deeper than 200 m shown in (a and b). (e) Time series of the simulated and observed potential water densities at the surface and bottom layers at the SM19 station near Hong Kong.
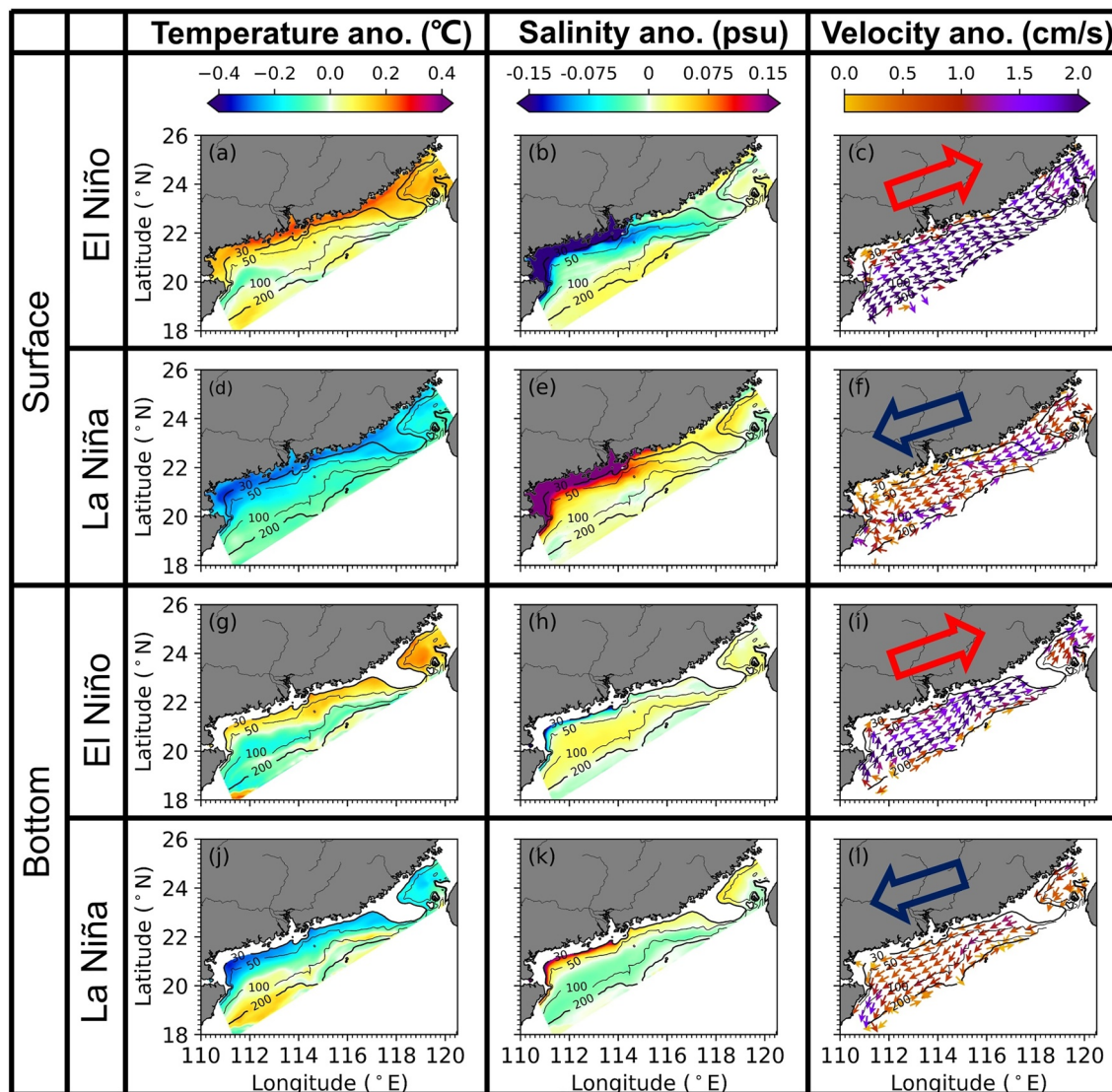
Figure 3. Composited temperature, salinity, and velocity anomalies in the upper 30 m of the water column in (a–c) El Niño and (d–f) La Niña years. (g–l) The same as (a–f), but for the bottom 30 m of the water column. In (g–l), waters shallower than 30 m are masked. Black contours indicate the 30, 50, 100, and 200 m isobaths. The thick arrows of the right last column indicate the principal directions of flow anomalies.

colder and less saline waters from the Taiwan Strait in winter. In La Niña years, the eastward extension of buoyant waters over the shelf and southwest of Taiwan Bank was significantly suppressed (Figure 3e).

In the lower layer, the general characteristics of the contrasting distributions of hydrographic properties and shelf circulation in El Niño and La Niña years were similar with those observed in the upper layer (Figures 3g–3l). Additionally, over the middle and outer shelf (i.e., seaward from the 50-m isobath), the waters in El Niño years were colder and more saline than those in La Niña years. This finding suggests that the water column over the shelf in El Niño years was more stratified than that in La Niña years due to the changes of the onshore intrusion from the slope in response to the ENSO. Thus, the extensive slope current, which is greatly dependent on the basin-scale atmospheric forcing and lateral current exchange through the Luzon Strait, is crucial for modulating the interannual variability of the shelf circulation; this aspect will be further explored.
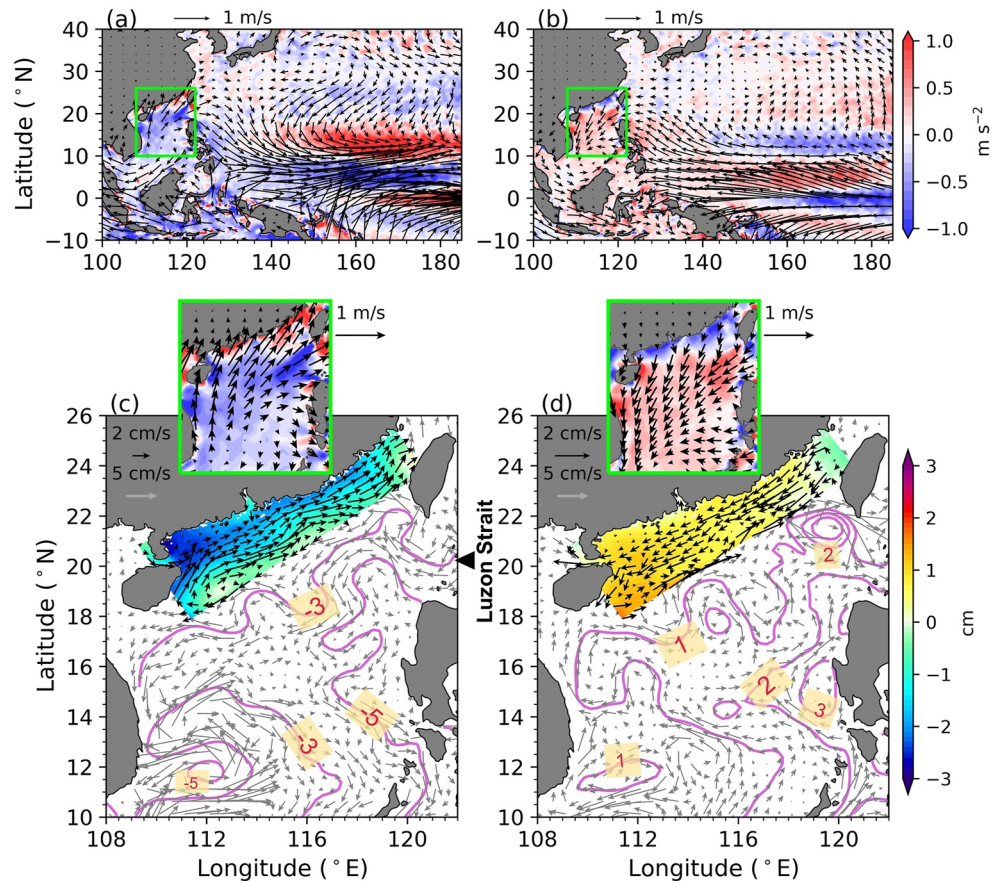
Figure 4. Composited wind anomaly and current anomaly in El Niño (a and c) and La Niña years (b and d) in the (a and b) northwestern Pacific Ocean and (c and d) South China Sea (SCS) basin. In (a and b), the wind-velocity anomaly (black arrows) and wind-stress curl anomaly (shading; unit: 10^{-11} m s^{-2}) computed from the ERA5 data set are shown. In (c and d), the basin-scale geostrophic current anomaly (gray arrows) and sea-level anomaly (SLA) (purple contours; unit: cm) from Copernicus Marine Environment Monitoring Service are superimposed. The simulated shelf-current anomaly (black arrows) and the SLA (shading) are superimposed over the northern SCS shelf. The corresponding wind-velocity anomalies are zoomed into the SCS basin (the green box in [a and b]) and placed on the top of (c and d). Note the different scales of black arrows for shelf current in (c and d).

4. Remote and Regional Forcings of the Interannual Variability of the NSCS Shelf Circulation

In the previous sections, we identified the remote and regional forcings modulating the interannual variability of the shelf circulation. To describe better the general patterns of the atmospheric forcings and SCS basin circulation in El Niño and La Niña years, we referred to the composited anomalies of wind-velocity, wind-stress curl, as well as SLA in the SCS basin and across the NSCS shelf in Figure 4. An AAC (cyclonic [AC]) wind with negative (positive) wind-stress curl anomaly was formed in El Niño (La Niña) years over the SCS basin (Figures 4a and 4b), possibly due to the propagation of atmospheric waves in the north tropics (e.g., B. Wang et al., 2000; L. Xie et al., 2016; S. P. Xie et al., 2016; Zhang et al., 2017), and the eastward (westward) motion of the warm pool in the northwestern Pacific Ocean. Consequently, a northeastward (southwestward) wind anomaly was generated over the NSCS shelf in El Niño (La Niña) years. The horizontal maps of the SLA and geostrophic velocity anomaly also indicated a strengthened (weakened) intrusion of Kuroshio current in the upper layer of the Luzon Strait in El Niño (La Niña) years (Figures 4c and 4d). In the following, we further investigate the specific roles of the remote and regional forcings in determining the interannual variability of the shelf current.
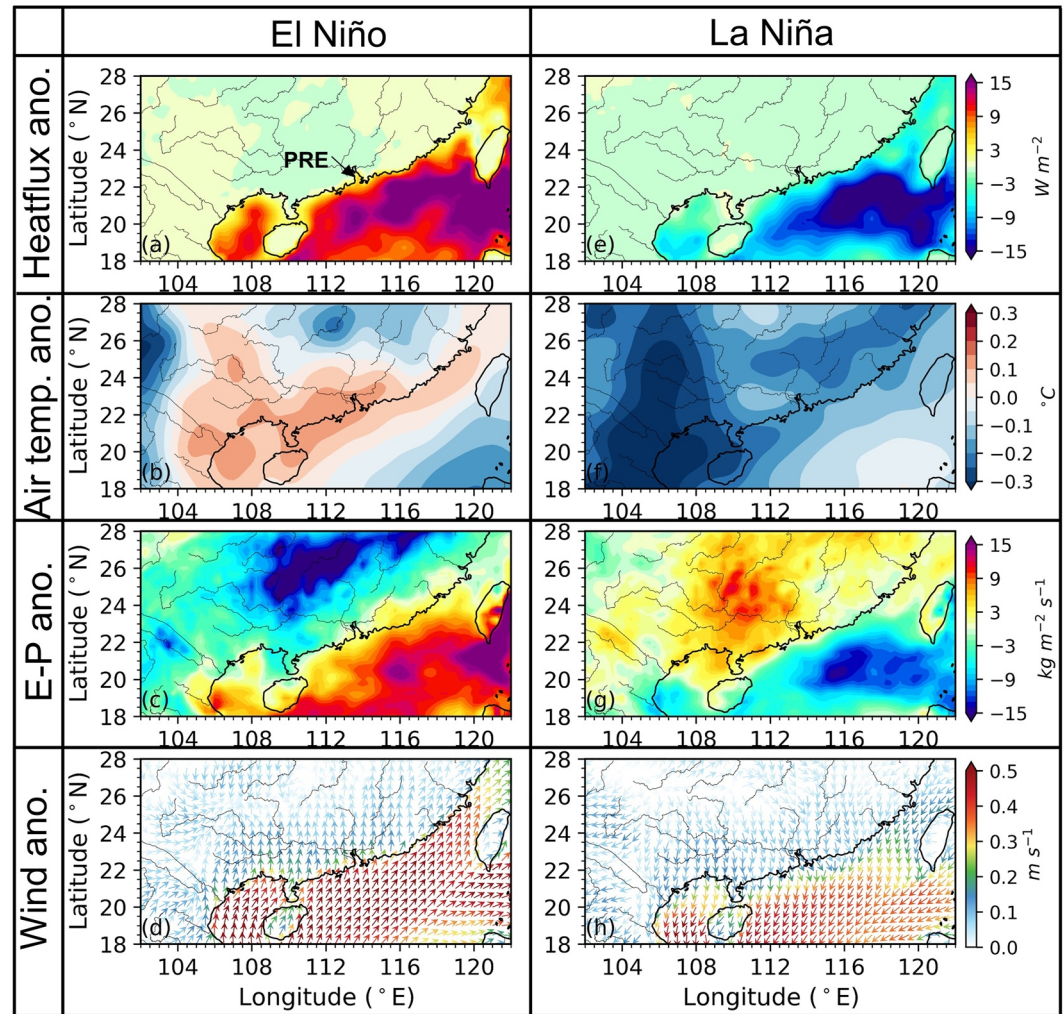
Figure 5. Net heat-flux (unit: W/m^2), 2-m air temperature (unit: °C), E–P (unit: 10^{-6} kg·m^{-2}·s^{-1}) and wind-velocity (unit: m/s) anomalies in El Niño years (a–d) and La Niña years (e–h).

4.1. Terrestrial Forcing

The hydrographic properties and circulation in the coastal areas are greatly impacted by the buoyant discharge from the neighboring PRE containing waters from the Pearl River catchment in the southern China. To eluci-date the impact of the changes of this buoyant discharge, we referred to the anomalies in net heat flux (NHF), air temperature at 2 m over the land and ocean surface, E–P, as well as the wind-velocity composited for the El Niño and La Niña years in Figure 5. A generally higher (lower) air temperature over the Pearl River catchment and the NSCS shelf in El Niño (La Niña) years is evident (Figures 5b and 5f). The distributions of NHF and air temperature clearly show mismatch in space, and considering the contrasting heat capacities of land and ocean, the interannual variability of the NHF over the NSCS sea surface was stronger than that over the land in southern China (Figures 5a and 5e). The horizontal maps of E–P anomalies further illustrate that the precipitation over the river basin in El Niño years was stronger than that in La Niña years (Figures 5c and 5g). Therefore, the distribu-tions of NHF, air temperature, and E–P anomalies show clearly that the buoyant water discharged into the PRE was intensified by the higher air temperature in El Niño years as compared to the case in La Niña years.

The fact that the air temperature was lower and evaporation was higher over the NSCS compared to their respec-tive values over the land in southern China is indicative of a northwestward atmospheric pressure-gradient force anomaly in El Niño years. This northwestward pressure-gradient force anomaly subsequently facilitated the north-eastward wind anomaly over the NSCS shelf (Figure 5d). The contrasting surface roughness of the sea surface

and land in southern China further stimulated the notable differences in wind speed and landward transport of evaporated moisture from the NSCS to southern China to increase precipitation over the Pearl River catchment (Figure 5c) (see also Li et al., 2021; Wei et al., 2020; Zhang et al., 2017). The subsequent increased discharge of warmer riverine buoyant water in El Niño years generated the observed less saline and warmer waters in the coastal areas west of the PRE (Figures 4a and 4b). The characteristics of the regional atmospheric forcings in La Niña years were, in general, mirrored with respect to those in El Niño years. However, given that the supply of moisture from the continent is weaker than that from the NSCS (Figure 5g), the intensity of the atmospheric circulation anomaly in La Niña years was weaker than that in El Niño years (Figure 5h).

The above results suggest that the response of the atmospheric circulation to the redistribution of heat and moisture in southern China and the NSCS amplifies the impacts of ENSO on the regional interannual climate variability. The impact of the atmospheric ENSO pathway on the upper-layer temperature and salinity variations across the NSCS shelf was thereby indirectly imposed by the establishment of a southwesterly (northeasterly) wind-stress anomaly over the shelf, through increased (decreased) river discharge due to strengthened precipitation (evaporation) over the Pearl River catchment, as well as increased (decreased) temperature of the riverine waters in El Niño (La Niña) years. These contrasting terrestrial processes contribute to the observed and simulated differences of temperature and salinity in the coastal seas to the shoreward from the 30 m isobath (Figure 3).

4.2. Regional Atmospheric Forcing

In the previous discussion, we showed that the dynamical impacts of the buoyant PRE waters are mainly limited in the coastal areas with less than 30 m depth, and the regional bathymetry is critical regarding the response of the regional climate to ENSO. The waters across the shelf between the 30 and 100 m isobaths exhibit contrasting circulation anomalies and coherence with the regional wind changes in El Niño and La Niña years (Figures 3 and 5). In this section, we elucidate the response of shelf currents to the interannual atmospheric circulation variability. To ensure the continuous estimation of the interannual variability in this complex dynamical system, we used the multi-variate empirical orthogonal functions (MVEOFs) analysis (Dawson, 2016) to synthesize the spatial and temporal variabilities of the concurrent wind and shelf-current variations. The orthogonal spatial modes (i.e., MVEOFs) were synthesized from four variables including the zonal and meridional components of wind and current, which incorporated the wind forcing and ocean circulation in their combined variances. Figure 6 shows the first two leading modes of MVEOF (hereafter, MVEOF1 and MVEOF2) between the winds over the NSCS and the shelf currents and their corresponding principal components (PCs; hereafter, PC1 and PC2). In each mode, the wind forcing and shelf circulation shared the same PC. The MVEOF1 and MVEOF2 modes accounted for 46% and 19% of the total variance, respectively. The MVEOF1 was manifested as along-shore wind stress pattern (which is linked with external forcing, as we show below), while the MVEOF2 was featured in the local wind stress anomaly.

The horizontal wind-velocity map of MVEOF1, as shown in Figure 6a, depicts clearly the previously discussed wind-field changes in accordance with ENSO (Section 4.1), for example, by revealing an evident northeastward anomaly over the shelf and stronger intensity over the slope east of the Hainan Island (Figure 6a). The NSCS circulation, in response to the interannual wind variability, exhibits a remarkable northeastward velocity anomaly over the shelf northeast of the Hainan Island (Figure 6c). The PC1 of MVEOF is highly consistent with the ONI, with 0.63 correlation coefficient (Figure 6e). Meanwhile, for most of the 25 years (i.e., except 2003–2006), the PC1 was in general varying in phase with the ONI. Specifically, the PC1 was positive not only in strong El Niño years, but also in normal years with positive ONI. The intensity of wind forcing, as well as shelf circulation in the NSCS, was greatly influenced by the ENSO.

The MVEOF2 of winds, as shown in Figure 6b, exhibits smaller scale spatial variability than that in Figure 6a. Over the outer shelf and slope to the east of Hainan, a southwestward wind anomaly is evident, while it gradually reverses to a northeastward wind anomaly over the shelf, seaward of the 200 m isobath (Figure 6b). This smaller scale wind anomaly, contributing to the formation of the stronger northeastward wind anomaly in El Niño years compared to that in La Niña years (Figures 5d and 5h), is similar with that in MVEOF1 over the shelf. In accordance with the wind MVEOF2 variability, an extensive southwestward slope current anomaly is stimulated, while the shelf and coastal currents generally exhibit northeastward velocity anomaly with much weaker intensity than that of the slope current (Figure 6d). This finding indicates that not only the basin-scale wind-stress variations over the SCS, but also the regional wind changes over the NSCS modulate the slope current. This regional
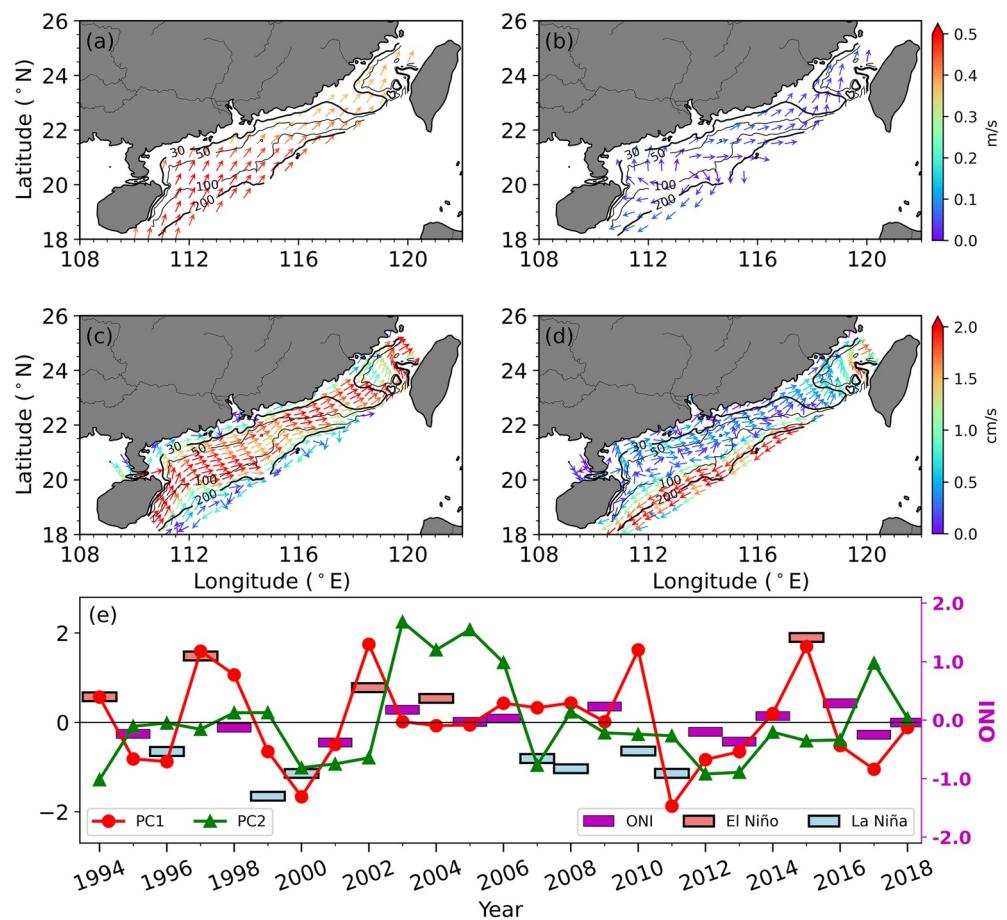
Figure 6. Multi-variate empirical orthogonal function decomposition of (a and b) wind-velocity (unit: m/s) and (c and d) depth-averaged shelf-current velocity (unit: cm/s), and (e) the corresponding principal component (PC) time series for the two leading modes. Black contours indicate the 30, 50, 100, and 200 m isobaths. In (e), the annually averaged Oceanic Niño Index (ONI) is also shown in colored caps.

wind-stress curl anomaly in years with negative PC2 phases seemed to facilitate the Qiongdong upwelling east of the Hainan Island, as mentioned by L. Xie et al. (2016) and S. P. Xie et al. (2016) The PC2, due to its smaller spatial scale compared to that of the MVEOF1 variability, is not highly correlated with the ONI (Figure 6e). A large positive anomaly of PC2 was observed in 2003–2006, when the coherency between the PC1 and ONI was hindered and the MVEOF1 variability was greatly suppressed. This finding suggests that the joint impacts of an extensive southwestward slope current and an anomalous northward intrusion into the Taiwan Strait could override the response of the shelf current to ENSO, when variability of the regional winds is secondary.

4.3. Oceanic Impacts of the Slope Currents

We have thus shown that the interannual variability of the NSCS shelf current is strongly modulated by the regional wind changes, which are not only highly related to the ENSO, but also to regional scale variability. In the following, we elucidate the interannual variability of the slope current, which acts as an important seaside boundary of the shelf current.

Figure 7 shows the first two leading MVEOF modes between the wind and SLA′ (i.e., spatial anomaly of the SLA) in the SCS. The SLA′ used here was calculated by SLA′ = SLA − $\overline{\text{SLA}}$, where $\overline{\text{SLA}}$ is the horizontally averaged SLA over the SCS basin. The MVEOF1, accounting for 30.7% of the total variance, shows a basin-scale SLA response to the large-scale wind-stress curl (Figures 7a and 7c). The negative (positive) wind-stress curl in years with positive (negative) PC1 phase was favorable for Ekman pumping (suction) and thus high (low) sea level inside the SCS basin. This stimulates a weaker (stronger) cyclonic circulation in the upper layer of the SCS
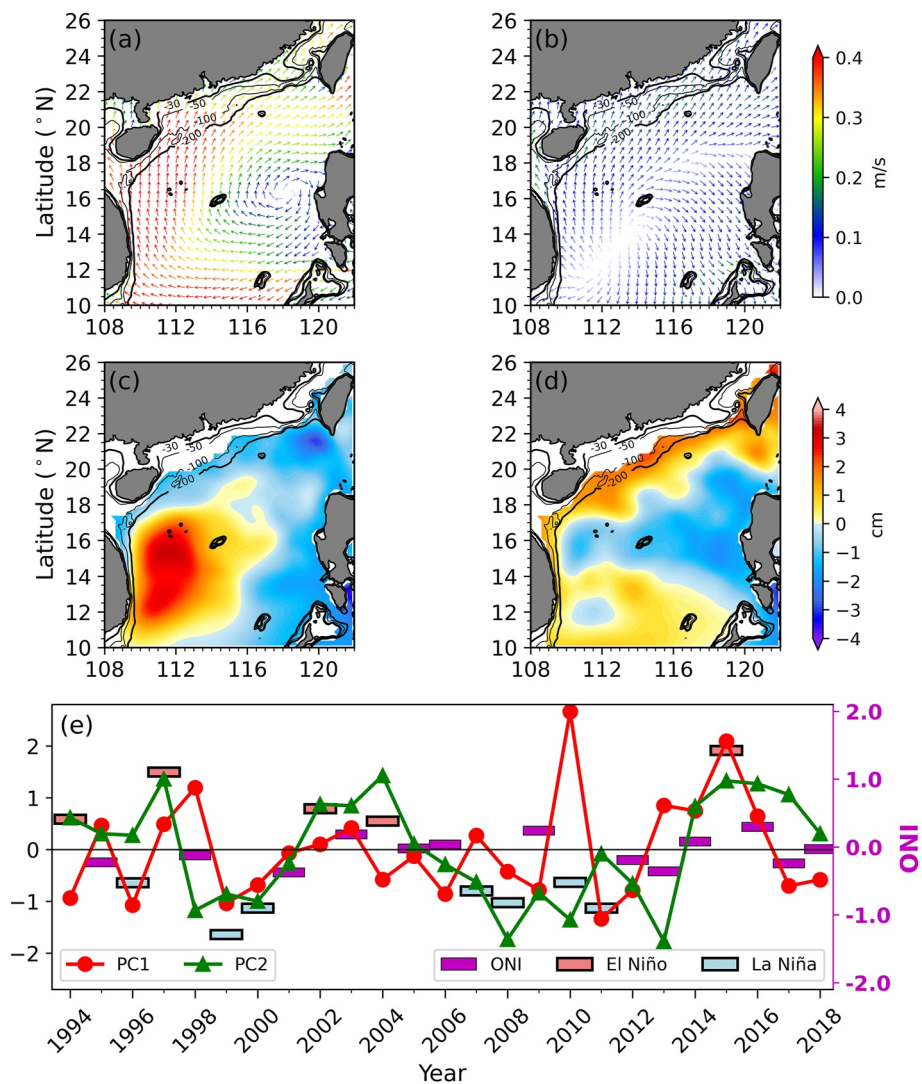
Figure 7. Multi-variate empirical orthogonal function decomposition of (a and b) wind velocities and (c and d) sea-level anomaly (SLA) anomaly over the South China Sea and (e) the corresponding principal component (PC) time series of the two leading modes. The SLA anomaly is the SLA removed by the basin-averaged SLA. Black contours indicate the 30, 50, 100, and 200 m isobaths. In (e), the annually averaged Oceanic Niño Index (ONI) is also shown in colored caps.

and a slope current in the NSCS through Sverdrup dynamics. This pattern is very similar to the MVEOF1 shown in Figure 6a, indicating the impacts of large-scale wind forcing on the NSCS slope current. The correlation coefficient between PC1 and ONI was 0.36 ($p < 0.1$), also implying that the ENSO-associated wind could impact the basin-scale sea level increase or decrease. In summer 2010 (Figure 7e), during the transition from an El Niño (i.e., 2009/2010) to a La Niña event (i.e., 2010/2011) (Chu et al., 2017; T. T. Zu et al., 2020), the anomalously high sea level inside the basin with the largest MVEOF1 amplitude was dominated by extreme sea-level distribution. The sea-level increase during 2005–2010 was facilitated by the strengthened negative wind-stress curl anomaly (i.e., AAC), with enhanced easterly trade winds over the sea south of 12°N and the enhanced westerly winds north of 12°N (W. D. Fang et al., 2014). However, the correlation coefficient between the PC1 and ONI was increased to 0.54 ($p < 0.01$) after excluding the extreme 2010 condition, indicating the complexity of ENSO. C. Z. Wang et al. (2006) and Y. G. Wang et al. (2006) showed that the first leading mode of either the anomalous anticyclonic wind-stress curl or the basin-scale upper layer circulation in the SCS confidently correlated with the ONI, which is consistent with our findings. Similar basin-scale anticyclonic/cyclonic patterns were found by G. H. Fang et al. (2006), W. D. Fang et al. (2006), and W. D. Fang et al. (2014), although their studies covered only the period extending to 2004 or 2010.

The MVEOF2, accounting for 18.2% of the total variance, exhibits similar spatial distribution with the MVEOF2 in Figure 6d, indicating the modulation of the NSCS shelf circulation by the slope current (Figures 7b and 7d). Interestingly, the time series of this PC2 variation is coherent with the ONI with 0.69 correlation coefficient at the 99% confidence level, and its spatial distribution reveals the connectivity of the slope current with the Kuroshio intrusion in the upper layer of the Luzon Strait. According to the previous investigations (e.g., J. P. Gan et al., 2016; J. Gan et al., 2022; Liu and Gan, 2017), the upper layer cyclonic slope current in the NSCS is largely related to the intrusion of positive planetary vorticity through Luzon Strait. The high correlation of the PC2 with the ONI and the spatial SLA distribution indicate an intensified westward intrusion of Kuroshio into the SCS in El Niño years, thus strengthening the southwestward slope current, as also shown in Figure 4 (see also Nan et al., 2015; Qu et al., 2004). In La Niña years, the Luzon Strait inflow is reduced, and the southwestward slope current is weakened accordingly. This high correlation indicates that the oceanic impact of the ENSO through the upper-layer Luzon Strait transport may overwhelm the atmospheric impact of the ENSO-associated AAC/AC anomaly on the slope current, which is shown clearly in the composited geostrophic flow anomaly in Figure 4, although the contribution of MVEOF2 to the total variance is smaller than that of MVEOF1. It is therefore evident that ENSO impacts are conveyed from both the atmospheric pathways through regulating the winds over the SCS basin and the oceanic pathways through altering the Kuroshio intrusion in the Luzon Strait.

When the spatial wind distribution in MVEOF2 is considered, it can be inferred that the observed higher SLA anomaly during the positive PC2 phase is associated with a northeastward wind anomaly over the slope. Given that the annually averaged winds blow southwestward over the shelf, with the center of the strongest wind speed being over the SCS slope (Figure 1a), a northeastward wind anomaly indicates a weakened positive wind-stress curl and intensified water convergence, establishing the enhanced SLA over the NSCS slope (Figures 7b and 7d). The enhanced southwestward slope current and northeastward anomaly of the NSCS shelf current is intensified during the positive PC2 phase and ONI—i.e., in the El Niño years—although the cyclonic basin circulation, represented by the SCSWBC (Figures 4c and 7c), is weakened. The established positive SLA anomaly over the slope facilitates the establishment of the northeastward shelf-velocity anomaly in the positive PC2 phase—i.e., in the El Niño years.

5. Conclusions

Combing long-term observations and a thoroughly validated numerical simulation, which was configured particularly for the complicated estuary–shelf–slope system in the NSCS, this study investigated the interannual variability of circulation and hydrographic properties in the NSCS, and discussed the coherence of the NSCS circulation with the regional climate changes in response to the ENSO influence through both atmospheric and oceanic pathways. The NSCS shelf circulation, in terms of both its hydrographic properties and velocity field, exhibited notable interannual variability associated with the impacts from ENSO. The schematics of the interannual variability of the NSCS shelf circulation were shown in Figure 8, by which we synthesized our major findings.

We generally showed that the interannual variability of the NSCS shelf current (i.e., between 30 and 200 m depth) responds asymmetrically to the atmospheric circulation in southern China and the NSCS, thereby exhibiting stronger (weaker) northeastward (southwestward) anomaly in El Niño (La Niña) years (Figure 8). Due to topography modulation around southern China and land–sea distributions in the NSCS, the northeastward wind anomaly over not only the NSCS shelf but also the Taiwan Strait is strengthened in El Niño years by regional wind-velocity scale changes. In coastal areas with less than 30 m depth, the response of the current and hydrographic properties is largely modulated by the buoyant waters from the Pearl River. In El Niño years, the buoyancy effect of warmer and less saline waters, due to the warmer precipitation from the atmosphere over the Pearl River catchment in southern China, weakens the northeastward flow anomaly by imposing a southwestward coastal current. Conversely, in La Niña years, the southwestward flow anomaly is also reduced, or even reversed, in the coastal areas west of the PRE due to the reduced riverine buoyant water.

The slope-current variability in the NSCS is primarily caused by wind-stress curl changes, and influenced by the strengthened/weakened intrusion of Kuroshio current in the Luzon Strait (Figure 8). In El Niño years, the cyclonic wind-stress curl over the SCS basin and the corresponding western boundary current is weakened (i.e., SCSWBC), but the secondary impact of this anticyclonic wind-velocity anomaly strengthens the Kuroshio intrusion through the Luzon Strait and enforces the southwestward slope current, as indicated by a positive SLA
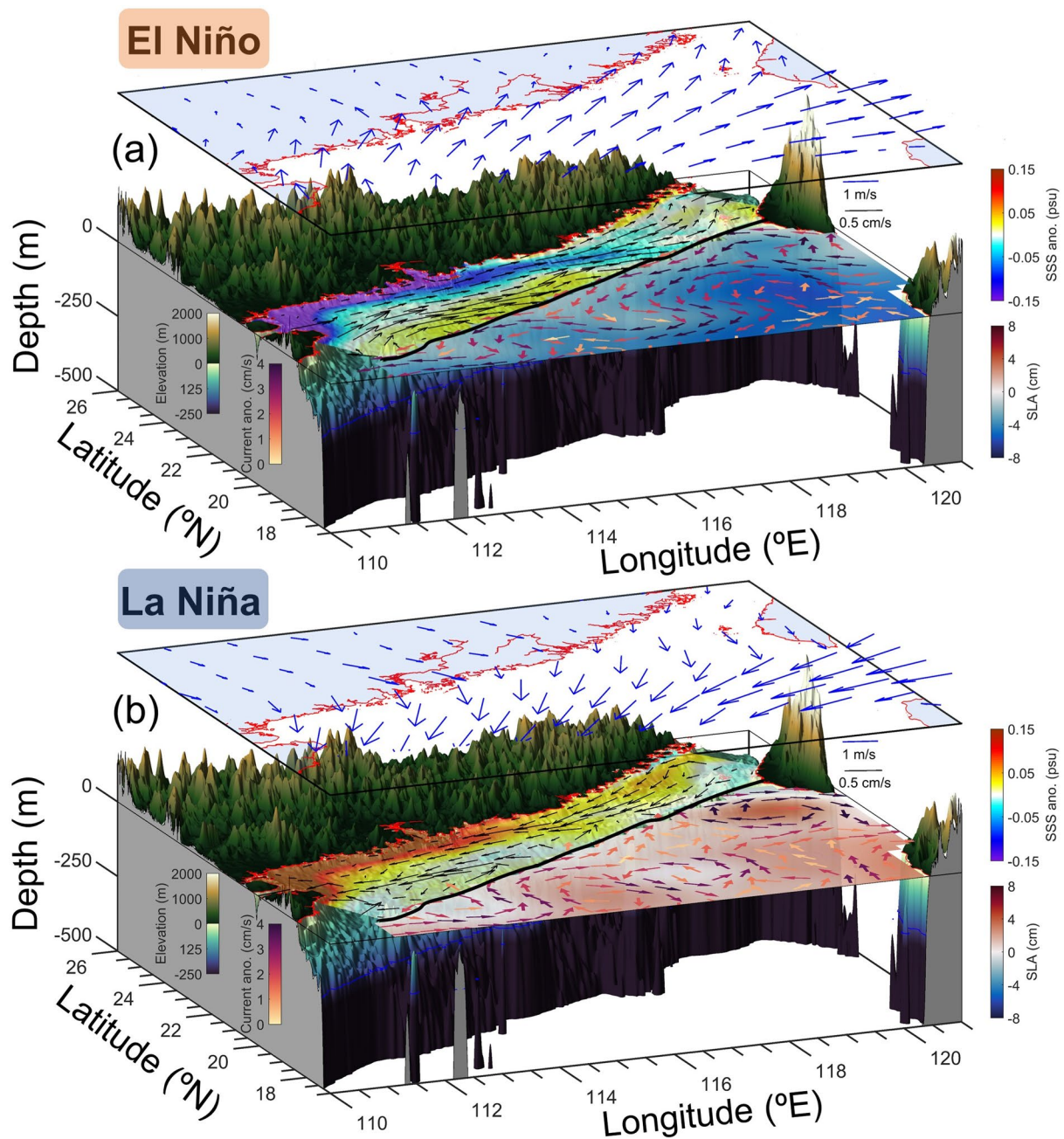
Figure 8. Schematic diagram of the interannual variability of the northern South China Sea shelf circulation and its climatic forcing factors in (a) El Niño and (b) La Niña years. Blue arrows indicate wind velocity anomalies; black arrows indicate shelf current anomalies. The elevation refers to the topography over land and ocean; the current anomaly in colored arrows refers to the geostrophic flow anomaly in the basin; the SLA refers to the sea-level anomaly in the basin; the SSS anomaly refers to the sea-surface salinity anomaly over the shelf.

anomaly over the NSCS slope. This established positive SLA in turn maintains the northeastward velocity anomaly over the NSCS shelf. The estuary–shelf–slope circulation patterns in La Niña years are generally mirrored with respect to those in El Niño years.

We note that, as this research mainly focused on the interannual variability of the shelf current, the interannual changes of synoptic scale processes regarding both the atmospheric (e.g., typhoons) and oceanic (e.g., eddies) forcings will be the focus of our future work. For example, the arrival of eddies over the shelf southwest of the Taiwan Strait has been reported to alter the water exchange in the Taiwan Strait (Chang et al., 2015). Earlier

studies, that is, Xu and Oey (2015) and Hong et al. (2000), also mentioned the role of baroclinic Rossby waves regarding sea-level changes in marginal areas. The governing dynamic mechanisms and processes linking the shelf circulation and tropical climate variability by propagation of planetary waves will also be our focus in the future.

Data Availability Statement

The time series of ensemble-mean sea-surface temperature and altimetry sea-level anomaly (SLA) from satellite remote sensing and the long-term observed hydrographic data in the surface and bottom layers of site SM19 in Hong Kong waters can be accessed at https://doi.org/10.6084/m9.figshare.17304239.v2. The atmospheric forcing used in this study are openly available from the European Centre for Medium-Range Weather Forecast ERA5 data set at https://doi.org/10.24381/cds.f17050d7. The gridded SLA and geostrophic velocities are openly available from Copernicus Marine Environment Monitoring Service at https://doi.org/10.48670/moi-00148.

References

Amante, C., & Eakins, B. W. (2009). Etopo1 1 arc-minute global relief model: Procedures, data sources and analysis. *The Psychologist*, *16*(3), 20–25. https://doi.org/10.7289/V5C8276M

Chang, Y. L., Miyazawa, Y., & Guo, X. Y. (2015). Effect of mesoscale eddies on the Taiwan Strait current. *Journal of Physical Oceanography*, *45*(6), 1651–1666. https://doi.org/10.1175/jpo-d-14-0248.1

Chu, X. Q., Dong, C. M., & Qi, Y. Q. (2017). The influence of ENSO on an oceanic eddy pair in the South China Sea. *Journal of Geophysical Research: Oceans*, *122*(3), 1643–1652.

Dawson, A. (2016). eofs: A library for EOF analysis of meteorological, oceanographic, and climate data. *Journal of Open Research Software*, *4*(1). https://doi.org/10.5334/jors.122

Egbert, G. D., & Erofeeva, S. Y. (2002). Efficient inverse modeling of barotropic ocean tides. *Journal of Atmospheric and Oceanic Technology*, *19*(2), 183–204. https://doi.org/10.1175/1520-0426(2002)019<0183:EIMOBO>2.0.CO;2

Fang, G. H., Chen, H. Y., Wei, Z. X., Wang, Y. G., Wang, X. Y., & Li, C. Y. (2006). Trends and interannual variability of the South China Sea surface winds, surface height, and surface temperature in the recent decade. *Journal of Geophysical Research*, *111*(C11). https://doi.org/10.1029/2005jc003276

Fang, W. D., Guo, J. J., Shi, P., & Mao, Q. W. (2006). Low frequency variability of South China Sea surface circulation from 11 years of satellite altimeter data. *Geophysical Research Letters*, *33*(22). https://doi.org/10.1029/2006gl027431

Fang, W. D., Qiu, F. W., & Guo, P. (2014). Summer circulation variability in the South China Sea during 2006-2010. *Journal of Marine Systems*, *137*, 47–54. https://doi.org/10.1016/j.jmarsys.2014.04.014

Gan, J., Kung, H., Cai, Z., Liu, Z., Hui, C., & Li, J. (2022). Hotspots of the stokes rotating circulation in a large marginal sea. *Nature Communications*, *13*(1), 2223. https://doi.org/10.1038/s41467-022-29610-z

Gan, J. P., Liu, Z. Q., & Hui, C. R. (2016). A three-layer alternating spinning circulation in the South China Sea. *Journal of Physical Oceanography*, *46*(8), 2309–2315.

Gan, J. P., Wang, J. J., Liang, L. L., Li, L., & Guo, X. G. (2015). A modeling study of the formation, maintenance, and relaxation of upwelling circulation on the northeastern South China Sea shelf. *Deep Sea Research Part II: Topical Studies in Oceanography*, *117*, 41–52. https://doi.org/10.1016/j.dsr2.2013.12.009

Hong, B., & Wang, D. (2008). Sensitivity study of the seasonal mean circulation in the northern South China Sea. *Advances in Atmospheric Sciences*, *25*(5), 824–840.

Hong, B. G., Sturges, W., & Clarke, A. J. (2000). Sea level on the U.S. East Coast: Decadal variability caused by open ocean wind-curl forcing. *Journal of Physical Oceanography*, *30*(8), 2088–2098. https://doi.org/10.1175/1520-0485(2000)030<2088:SLOTUS>2.0.CO;2

Jing, Z. Y., Qi, Y. Q., & Du, Y. (2011). Upwelling in the continental shelf of northern South China Sea associated with 1997-1998 El Nino. *Journal of Geophysical Research*, *116*(C2). https://doi.org/10.1029/2010jc006598

Li, X. T., Wang, C. Z., & Lan, J. (2021). Role of the South China Sea in Southern China rainfall: Meridional moisture flux transport. *Climate Dynamics*, *56*(7–8), 2551–2568. https://doi.org/10.1007/s00382-020-05603-w

Liu, C. L., Li, X., Wang, S. F., Tang, D. L., & Zhu, D. H. (2020). Interannual variability and trends in sea surface temperature, sea surface wind, and sea level anomaly in the South China Sea. *International Journal of Remote Sensing*, *41*(11), 4160–4173. https://doi.org/10.1080/01431161.2020.1714777

Liu, J., Dai, J. J., Xu, D. F., Wang, J., & Yuan, Y. P. (2018). Seasonal and interannual variability in coastal circulations in the northern South China Sea. *Water*, *10*(4). https://doi.org/10.3390/w10040520

Liu, N., Geng, B. X., Xue, H. J., Xiu, P., Wang, Q., & Wang, D. X. (2020). Interannual variability of shelf and slope circulations in the northern South China Sea. *Journal of Ocean University of China*, *19*(5), 1005–1016. https://doi.org/10.1007/s11802-020-4446-9

Liu, Q., Huang, R., & Wang, D. (2011). Implication of the South China Sea throughflow for the interannual variability of the regional upper-ocean heat content. *Advances in Atmospheric Sciences*, *29*(1), 54–62. https://doi.org/10.1007/s00376-011-0068-x

Liu, Z. Q., & Gan, J. P. (2016). Open boundary conditions for tidally and subtidally forced circulation in a limited-area coastal model using the Regional Ocean Modeling System (ROMS). *Journal of Geophysical Research: Oceans*, *121*(8), 6184–6203. https://doi.org/10.1002/2016JC011975

Liu, Z. Q., & Gan, J. P. (2017). Three-dimensional pathways of water masses in the South China Sea: A modeling study. *Journal of Geophysical Research: Oceans*, *122*(7), 6039–6054. https://doi.org/10.1002/2016JC012511

Liu, Z. Q., & Gan, J. P. (2020). A modeling study of estuarine-shelf circulation using a composite tidal and subtidal open boundary condition. *Ocean Modelling*, *147*, 101563. https://doi.org/10.1016/j.ocemod.2019.101563

Liu, Z. Q., Zu, T. T., & Gan, J. P. (2020). Dynamics of cross-shelf water exchanges off Pearl River Estuary in summer. *Progress in Oceanography*, *189*, 102465. https://doi.org/10.1016/j.pocean.2020.102465

Lui, H. K., Chen, C. T. A., Hou, W. P., Liau, J. M., Chou, W. C., Wang, Y. L., et al. (2020). Intrusion of Kuroshio helps to diminish coastal hypoxia in the coast of northern South China Sea. *Frontiers in Marine Science*, *7*(788). https://doi.org/10.3389/fmars.2020.565952

Mao, Q., Shi, P., Yin, K., Gan, J., & Qi, Y. (2004). Tides and tidal currents in the Pearl River Estuary. *Continental Shelf Research*, *24*(16), 1797–1808. https://doi.org/10.1016/j.csr.2004.06.008

Mellor, G. L., & Yamada, T. (1982). Development of a turbulence closure-model for geophysical fluid problems. *Reviews of Geophysics*, *20*(4), 851–875. https://doi.org/10.1029/RG020i004p00851

Nan, F., Xue, H. J., & Yu, F. (2015). Kuroshio intrusion into the South China Sea: A review. *Progress in Oceanography*, *137*, 314–333. https://doi.org/10.1016/j.pocean.2014.05.012

Ou, S. Y., Zhang, H., & Wang, D. X. (2009). Dynamics of the buoyant plume off the Pearl River Estuary in summer. *Environmental Fluid Mechanics*, *9*(5), 471–492. https://doi.org/10.1007/s10652-009-9146-3

Qian, W., Gan, J. P., Liu, J. W., He, B. Y., Lu, Z. M., Guo, X. H., et al. (2018). Current status of emerging hypoxia in a eutrophic estuary: The lower reach of the Pearl River Estuary, China. *Estuarine, Coastal and Shelf Science*, *205*, 58–67. https://doi.org/10.1016/j.ecss.2018.03.004

Qu, T., Kim, Y. Y., Yaremchuk, M., Tozuka, T., Ishida, A., & Yamagata, T. (2004). Can Luzon Strait transport play a role in conveying the impact of ENSO to the South China Sea? *Journal of Climate*, *17*(18), 3644–3657. https://doi.org/10.1175/1520-0442(2004)017<3644:CLSTPA>2.0.CO;2

Quan, Q., Xue, H. J., Qin, H. L., Zeng, X. Z., & Peng, S. Q. (2016). Features and variability of the South China Sea western boundary current from 1992 to 2011. *Ocean Dynamics*, *66*(6–7), 795–810. https://doi.org/10.1007/s10236-016-0951-1

Rong, Z. R., Liu, Y. G., Zong, H. B., & Cheng, Y. C. (2007). Interannual sea level variability in the South China Sea and its response to ENSO. *Global and Planetary Change*, *55*(4), 257–272. https://doi.org/10.1016/j.gloplacha.2006.08.001

Shchepetkin, A. F., & McWilliams, J. C. (2005). The regional oceanic modeling system (ROMS): A split-explicit, free-surface, topography-following-coordinate oceanic model. *Ocean Modelling*, *9*(4), 347–404. https://doi.org/10.1016/j.ocemod.2004.08.002

Shu, Y. Q., Wang, Q., & Zu, T. T. (2018). Progress on shelf and slope circulation in the northern South China Sea. *Science China Earth Sciences*, *61*(5), 560–571. https://doi.org/10.1007/s11430-017-9152-y

Smolarkiewicz, P. K. (1984). A fully multidimensional positive definite advection transport algorithm with small implicit diffusion. *Journal of Computational Physics*, *54*(2), 325–362. https://doi.org/10.1016/0021-9991(84)90121-9

Song, Y., & Haidvogel, D. (1994). A semi-implicit ocean circulation model using a generalized topography-following coordinate system. *Journal of Computational Physics*, *115*(1), 228–244. https://doi.org/10.1006/jcph.1994.1189

Sun, Y., & Lan, J. (2021). Summertime eastward jet and its relationship with western boundary current in the South China Sea on the interannual scale. *Climate Dynamics*, *56*(3–4), 935–947. https://doi.org/10.1007/s00382-020-05511-z

Wang, B., Wu, R. G., & Fu, X. (2000). Pacific–East Asian teleconnection: How does ENSO affect East Asian climate? *Journal of Climate*, *13*(9), 1517–1536. https://doi.org/10.1175/1520-0442(2000)013<1517:PEATHD>2.0.CO;2

Wang, C. Z., Wang, W. Q., Wang, D. X., & Wang, Q. (2006). Interannual variability of the South China Sea associated with El Nino. *Journal of Geophysical Research*, *111*(C3). https://doi.org/10.1029/2005jc003333

Wang, Q., Zeng, L. L., Shu, Y. Q., Liu, Q. Y., Zu, T. T., Li, J., et al. (2020). Interannual variability of South China Sea winter circulation: Response to Luzon Strait transport and El Nino wind. *Climate Dynamics*, *54*(1–2), 1145–1159. https://doi.org/10.1007/s00382-019-05050-2

Wang, Y. G., Fang, G. H., Wei, Z. X., Qiao, F. L., & Chen, H. Y. (2006). Interannual variation of the South China Sea circulation and its relation to El Nino, as seen from a variable grid global ocean model. *Journal of Geophysical Research*, *111*(C11). https://doi.org/10.1029/2005jc003269

Wei, X., Cai, S., Ni, P., & Zhan, W. (2020). Impacts of climate change and human activities on the water discharge and sediment load of the Pearl River, Southern China. *Scientific Reports*, *10*(1), 16743. https://doi.org/10.1038/s41598-020-73939-8

Xie, L., Zong, X., Yi, X., & Li, M. (2016). The interannual variation and long-term trend of Qiongdong upwelling. *Oceanologia et Limnologia Sinica*, *47*(1), 43–51. (in Chinese with English abstract). https://doi.org/10.11693/hyhz20150300069

Xie, S. P., Kosaka, Y., Du, Y., Hu, K. M., Chowdary, J., & Huang, G. (2016). Indo-western Pacific ocean capacitor and coherent climate anomalies in post-ENSO summer: A review. *Advances in Atmospheric Sciences*, *33*(4), 411–432.

Xu, F. H., & Oey, L. Y. (2015). Seasonal SSH variability of the northern South China Sea. *Journal of Physical Oceanography*, *45*(6), 1595–1609. https://doi.org/10.1175/JPO-D-14-0193.1

Xue, H. J., Chai, F., Pettigrew, N., Xu, D. Y., Shi, M., & Xu, J. P. (2004). Kuroshio intrusion and the circulation in the South China Sea. *Journal of Geophysical Research*, *109*(C2). https://doi.org/10.1029/2002jc001724

Yan, Y. F., Qi, Y. Q., & Zhou, W. (2010). Interannual heat content variability in the South China Sea and its response to ENSO. *Dynamics of Atmospheres and Oceans*, *50*(3), 400–414. https://doi.org/10.1016/j.dynatmoce.2010.07.002

Yuan, Y. C., Liao, G. H., & Xu, X. H. (2007). Three dimensional diagnostic modeling study of the South China Sea circulation before onset of summer monsoon in 1998. *Journal of Oceanography*, *63*(1), 77–100. https://doi.org/10.1007/s10872-007-0007-8

Yuan, Y. C., Liao, G. H., & Yang, C. H. (2009). A diagnostic calculation of the circulation in the upper and middle layers of the Luzon Strait and the northern South China Sea during March 1992. *Dynamics of Atmospheres and Oceans*, *47*(1–3), 86–113. https://doi.org/10.1016/j.dynatmoce.2008.10.005

Zhang, R. H., Min, Q. Y., & Su, J. Z. (2017). Impact of El Nino on atmospheric circulations over East Asia and rainfall in China: Role of the anomalous western North Pacific anticyclone. *Science China Earth Sciences*, *60*(6), 1124–1132. https://doi.org/10.1007/s11430-016-9026-x

Zhu, X. H., Zhao, R. X., Guo, X. Y., Long, Y., Ma, Y. L., & Fan, X. P. (2015). A long-term volume transport time series estimated by combining in situ observation and satellite altimeter data in the northern South China Sea. *Journal of Oceanography*, *71*(6), 663–673. https://doi.org/10.1007/s10872-015-0305-5

Zu, T., Xue, H., Wang, D., Geng, B., Zeng, L., Liu, Q., et al. (2018). Interannual variation of the South China Sea circulation during winter: Intensified in the southern basin. *Climate Dynamics*, *52*(3–4), 1917–1933. https://doi.org/10.1007/s00382-018-4230-3

Zu, T. T., Gan, H. P., & Erofeeva, S. Y. (2008). Numerical study of the tide and tidal dynamics in the South China Sea. *Deep Sea Research Part I: Oceanographic Research Papers*, *55*(2), 137–154. https://doi.org/10.1016/j.dsr.2007.10.007

Zu, T. T., Wang, D. X., Wang, Q., Li, M. T., Wei, J., Geng, B. X., et al. (2020). A revisit of the interannual variation of the South China Sea upper layer circulation in summer: Correlation between the eastward jet and northward branch. *Climate Dynamics*, *54*(1–2), 457–471. https://doi.org/10.1007/s00382-019-05007-5